Nanoscale

Accepted Manuscript

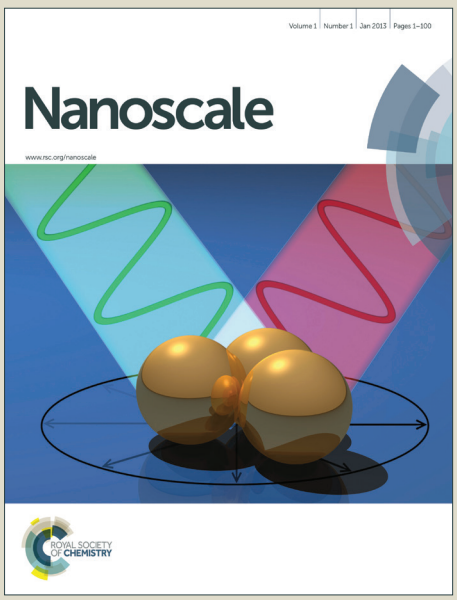

ROYAL SOCIETY OF CHEMISTRY

www.rsc.org/nanoscale

Journal Name

ARTICLE TYPE

Cite this: DOI: 10.1039/xxxxxxxxxx

Enhancing carrier generation in TiO2 by a synergistic effect between plasmon resonance in Ag nanoparticles and optical interference

Giuseppe Cacciato,[a,b] Maxime Bayle,[c] Alessandro Pugliara,[c] Caroline Bonafos,[c] Massimo Zimbone,[b] Vittorio Privitera,[b] Maria Grazia Grimaldi,[a] Robert Carles[c,*]

Received Date
Accepted Date

DOI: 10.1039/xxxxxxxxxx

www.rsc.org/journalname

Silver nanoparticles have been embedded at a few nanometer distance from the free surface of titania/silica multilayers using low energy ion beam synthesis. Transmission electron microscopy shows the presence of 3 nm-sized crystalline particles. Reflectance spectroscopy on these composite substrates shows an increase of the light capture efficiency in the visible range. This behaviour is interpreted as a synergistic effect between plasmon polariton resonance and Fabry-Perot interferences. Plasmon-resonant Raman spectroscopy is deeply used to analyze, on one hand confinement of vibrations and electronic excitations in Ag NPs, and on the other hand coupling of polar TiO_2 phonons with injected photo-generated carriers. It is shown how these new Ag/TiO_2 nanocomposite films appear as very promising to enhance the efficiency and enlarge the spectral sensitivity of plasmo-electronics devices.

1 Introduction

Great efforts have been recently devoted to developing heterogeneous photocatalysts for various environmental applications[1–3]. Whatever the application, such as water or air purification, solar energy conversion from water splitting[4]..., photocatalytic reactions are always the result of complex and concurring processes occurring at the nanoscale. These processes are: *(i)* the absorption of light creating electron-hole excitations in a thin film of a semiconducting compound, *(ii)* the separation followed by *(iii)* the transfer of these charges to the free surface in contact with water or air, *(iv)* their interaction with organic or inorganic molecules located on this surface through oxidation and reduction reactions, leading finally *(v)* the electronic system to recover its ground state. Among semiconductor-based photocatalysts, titania (TiO_2) has received great attention due to its abundance, chemical stability, low toxicity, high efficiency and cheapness[5].

In order to enhance the efficiency of the preceding processes (from *i* to *iv*), surface-plasmon mediated photocatalytic activity of TiO_2 has become a hot research topic[6–13]. When metallic nanoparticles (NPs) are embedded in a titania matrix, the incident light induces a collective oscillation of the free electrons of these NPs at the so-called localized surface plasmon-polariton resonance (LSPR). Near the frequency of this resonance and in the immediate vicinity of the NPs the confinement of light is enhanced boosting the creation of high energy electron-hole pairs (*i*) into the metallic NPs because of the rapid (*i.e.* within few femtoseconds) plasmon dephasing decay according to the so-called Landau damping mechanism. Studies of metal-modified TiO_2 photocatalysts[6,7,14,15] have shown that the formation of a Shottky barrier at the metal/semiconductor interface promotes an efficient separation (*ii*) of the photogenerated electrons and holes. In particular it has been shown that silver nanoparticles (Ag NPs) deposited on TiO_2 act as electron traps, enhancing this separation and the subsequent transfer (*iii*) of electrons to a molecule acting as an acceptor[8,16].

To improve the performance of the photocatalytis, devices need to be designed with plasmonic substrates[17] that can effectively absorb the entire solar spectrum (*i*), thus harvesting energy from sunlight. As a matter of fact doping TiO_2 with small Ag NPs can enhance its photocatalytic activity under UV light due to intrinsic intraband electronic transitions in silver, as well as promote the optical response of TiO_2 in the visible range due to intraband transitions via LSPR. Interaction of photons with these metal-dielectric nanocomposite films then supports plasmon-enhanced processes in the visible range. In this respect, Surface Enhanced Raman scattering (SERS) can be used as a very efficient gauge of this phenomenon because the electron-photon interaction happens twice, for incident and scattered photons. Since scattering processes concern both vibrational and electronic excitations, Ra-

[a] *Dipartimento di Fisica ed Astronomia-Università di Catania, via S. Sofia 64, 95123 Catania, Italy.*
[b] *CNR-IMM, via S. Sofia 64, 95123 Catania, Italy.*
[c] *CEMES-CNRS Université de Toulouse, 29 rue Jeanne Marvig, BP 94347, 31055 Toulouse Cedex 4, France.*
∗ Corresponding author : Robert Carles, e-mail : robert.carles@cemes.fr

man spectroscopy gives signatures of both arrangements of atoms and photo-generation of carriers[18].

In this work we report on the design, fabrication and analysis of a novel class of Ag/TiO_2 nanocomposite film produced by low-energy ion beam synthesis (LE-IBS). Ag NPs assemblies are buried inside a dielectric TiO_2 layer at only few nanometers below its free surface. Such a small distance is of prime importance for the previously described steps by reducing recombination of charges during their transfer (*iii*) and eventually activating chemical reactions through a localized heating in the active zone (*iv*). A strong enhancement of the LSPR and its tuning in the middle of the visible range is obtained because of the high value of the refractive index of TiO_2 ($n_{TiO_2,vis} \approx 2.7$ in the visible range). By changing the embedding medium from SiO_2 ($n_{SiO_2} \approx 1.5$) to TiO_2 the LSPR of Ag NPs shift from the near UV range (≈ 400 nm) to the visible range (≈ 590 nm), as shown in Fig. 1. In this figure, the extinction coefficient has been calculated for a spherical Ag NP with a diameter $D = 3$ nm. The details of the model are given in the Supplementary file. Owing to the fact that the higher the refractive index, the better is the electromagnetic energy confinement, the quality factor of the LSPR is doubled when changing SiO_2 to TiO_2.

Engineering the architecture of the stacking layers have been demonstrated as a key to take simultaneously advantage of spectrally and spatially LSPR but also of optical amplification. This has been recently proposed for enhanced spectroscopy and imaging[19]. By choosing an appropriate thickness of a TiO_2 layer deposited on a silicon substrate, one can easily tune the spectral positions of one of the antireflective minima and LSPR, as shown in Fig. 1. The model used for calculating the reflectance response is presented in the Supplementary file. The aim of this work is to take benefit of this phenomenon in multilayer stacking containing TiO_2 and embedding Ag NPs. They will be adapted to manage amplifying processes in the visible range by exploiting simultaneously the resulting optical interference phenomenon and LSPR.

In addition to structural and optical characterizations using transmission electron microscopy (TEM) and reflectance spectroscopy, plasmon-resonant Raman spectroscopy has been more deeply used in this work to analyze confinement of vibrations in embedded Ag NPs and coupling of polar TiO_2 phonons with photo-generated carriers. We show how this new Ag/TiO_2 nanocomposite film can be an efficient way to enhance and spectrally enlarge the photo-catalytic efficiency of TiO_2.

2 Materials and Methods

2.1 Elaboration

TiO_2 has been obtained by thermal oxidation (600 °C, 30 min in 2.5 lpm of O_2 flow using a standard Carbolite horizontal furnace) of Ti films grown by DC sputtering ($P = 3$ kW, Ar flow = 48 sccm, low pressure 10^{-3} mbar) on thermally oxidized Si wafers. The SiO_2 layer thickness was 85 nm and two Ti film thicknesses (50 and 100 nm) were chosen so that, after oxidation, we obtained correspondingly around 90 nm and 165 nm TiO_2 films, referred as sample A and B, respectively.

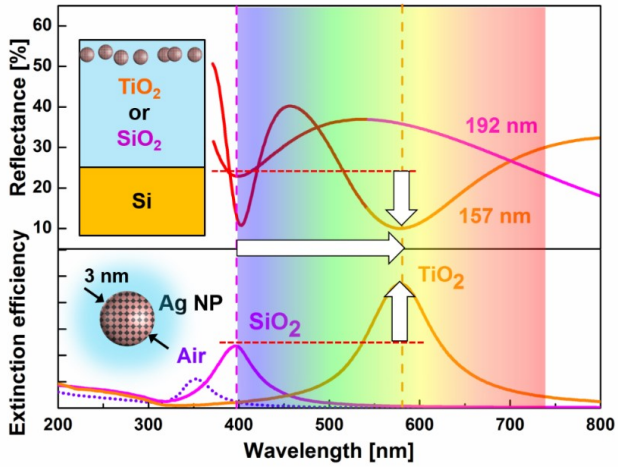

Fig. 1 Theoretical simulation illustrating the tuning of anti-reflectivity condition in a SiO_2 (or TiO_2)/Si heterostructure and LSPR in a silver nanoparticle of diameter $D = 3$ nm.

Silver ions (Ag^+) have been implanted in the TiO_2 layer with low energy (20 keV) and a fluence of 3×10^{16} ions cm^{-2} by means of a Varian 200A2 implanter. According to SRIM simulations[20] the implanted profile is expected to reach its maximum at a depth of 10 nm with a straggle of 2.5 nm. A part of the free surface has been masked during implantation to get a reference signal in order to check the plasmon resonance effect on vibrations and carriers in the TiO_2 layer.

2.2 Structural and chemical analysis

The composition and thickness of the films, before and after implantation, were checked by Rutherford Backscattering Spectrometry (RBS), with a 3.5 MeV HVEE Singletron accelerator, using a 2 MeV He^+ beam with a scattering angle of 165° in normal incidence.

Microscopy imaging was performed using a field emission Transmission Electron Microscope, FEI Tecnai^{TM} F20 microscope operating at 200 kV, equipped with a spherical aberration corrector dedicated for high quality High Resolution Electron Microscopy (HREM) images with an increased signal/noise ratio and nearly no delocalization effect at surfaces and interfaces. Energy Filtered TEM (EFTEM) imaging was conducted with a TRIDIEM Gatan imaging filter attached to the microscope and coupled to a scanning stage for the STEM-EELS analyses. TEM lamellae transparent to electrons were prepared in cross-section by mechanical grinding and Ar^+ ion milling.

2.3 Optical spectrometry

The UV-VIS optical characterization was obtained by extracting 6° reflectance spectra in the 200-800 nm wavelength range, by using a Varian Cary 500 double beam scanning UV/VIS/NIR spectrophotometer. Raman spectra were recorded over a wide frequency range using an XploRA Horiba Jobin Yvon spectrometer.

The laser illumination at 532 or 638 nm was lower than 1 mW to avoid any heating of the sample. Some very low frequency Raman-Brillouin spectra were recorded using a specifically modified version of a T64000 Horiba Jobin Yvon spectrometer and a Krypton laser tuned at the 530 nm line.

2.4 Photocatalysis

For the discoloration tests we referred to the guidelines of the ISO 10678:2010[21]. According to the standard, 10 μL of methylene blue (MB) solution (0.05 wt%) were added to each 1 mL volume of deionized Milli-Q water (resistivity 18 MΩcm). The MB concentrations were measured according to the Lambert-Beer law at 664 nm (extinction coefficient $7.4\times10^{-4}\,M^{-1}cm^{-1}$). During the tests, each sample was placed on the bottom of a circular vessel of 2 cm^2 filled with 2 mL of the MB-water solution. The solutions were left for one hour in dark to allow the absorption of MB onto film and vessels surfaces and then illuminated with UV or visible (blue) light. During light irradiation the vessels were covered with quartz in order to avoid evaporation during irradiation. The wavelength of the UV light source was centered at 368 nm (FWHM lower than 10 nm) and UV irradiance was 1.1 $mWcm^{-2}$. The wavelength of the visible light source was centered at 453 nm (FWHM 40nm) and irradiance was 1.5 $mWcm^{-2}$. In this latter experimental condition, a UV filter was used in order to cut the wavelengths below 420 nm. The degradation rate was measured along time.

3 Results and discussion

3.1 Structural characterization: RBS and TEM imaging

The thicknesses (90 ± 4 nm and 165 ± 4 nm for sample A and B, respectively) and the stoichiometry ($[O]/[Ti]=2.0\pm0.1$) of the bare TiO_2 substrates before implantation were extracted by RBS (not shown). Moreover, since RBS is sensitive to Ag dissolved in the matrix, even if not clustered, it was possible to evaluate the amount of Ag after implantation. Thus the analysis of the Ag peak resulted in $1.1\pm0.1\,at\,cm^{-2}$ dispersed in 18 ± 2 nm of TiO_2 matrix. The measured thicknesses of titania layers after implantation were respectively 83 ± 4 nm and 161 ± 4 nm. This result, together with a reduced dose of Ag in the matrix, can be explained by some sputtering occurred during implantation.

A cross-section Bright Field TEM image of sample A at low magnification (Fig. 2) shows the stacking of two layers on top of a Si substrate: TiO_2 with thickness $t_{TiO_2}=91\pm4$ nm deposited on SiO_2 ($t_{SiO_2}=84\pm3$ nm). In the region close to the surface the presence of a band of nanoparticles is detected, with average diameter $D=3$ nm (see Figs 2 and 3a). The Ag NPs have nucleated during the implantation process and no annealing procedure was necessary for the phase separation, as already observed for a SiO_2 matrix[22]. The Ag NPs are located in a 14 ± 1 nm thick band near the free surface. This is in good agreement with the SRIM simulations of the implanted profile, which peaks at a depth of 10 nm with a straggle of 2.5 nm. The region damaged by the implantation process, referred in what follows as *amorphous-like* TiO_2 ($a-TiO_2$), is around 20 nm thick.

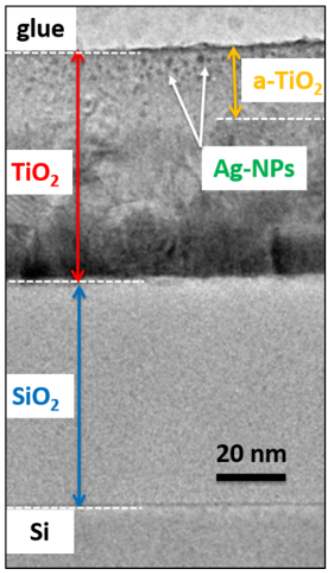

Fig. 2 TEM cross-section image of sample A, observed in defocused Bright Field, showing the different stacked layers.

3.2 UV-visible optical response: plasmonic-optical enhancement

The reflectance spectrum of a non-implanted zone of sample A is reported in Fig. 4a. The two minima around 500 nm and 350 nm correspond to anti-reflective conditions. As a matter of fact, the anti-reflective condition is given by the following equation:

$$2(n_{TiO_2}t_{TiO_2}+n_{SiO_2}t_{SiO_2})=(m+1/2)\lambda_m \qquad (1)$$

Using the thicknesses determined by TEM, one gets $\lambda_{1,A}=496$ nm with $n_{TiO_2,vis}\approx2.7$ and $\lambda_{2,A}=371$ nm with $n_{TiO_2,UV}\approx3.7$ for the destructive interference order $m=1$ and 2, respectively, in good agreement with experiment. One has to take in mind that the latter wavelength is located in the UV range where TiO_2 is strongly absorbing below its gap, *i.e.* 407 nm (or 354 nm) for rutile (or anatase, respectively)[23].

To account more quantitatively of the optical response, we performed calculations of the reflectance. The theoretical spectra were obtained by describing the propagation of electromagnetic waves in the stratified medium using a matrix formulation[18,19] and using the refractive and extinction indexes of amorphous SiO_2 and crystalline TiO_2 as input data. The best fit reported in Fig. 4a was obtained with $t_{TiO_2}=89$ nm and $t_{SiO_2}=84$ nm, in perfect agreement with TEM data. The experimental record of the reflectance is very well accounted for, in particular in the UV range (200-400 nm) where the absorption effect dominates.

The reflectance spectrum recorded from an implanted zone of sample A is reported in Fig. 4b. The presence of silver induces a spectral widening and blue shift (50 nm), and a reinforcing (up to 60%) of the anti-reflective effect in the visible range. The LSPR should occur around 590 nm for Ag NPs embedded in a crystalline TiO_2 matrix (see Fig. 1), but its location is not obvious to determine from experimental data, because the resonance effect strongly interferes with the signature of electromagnetic confine-

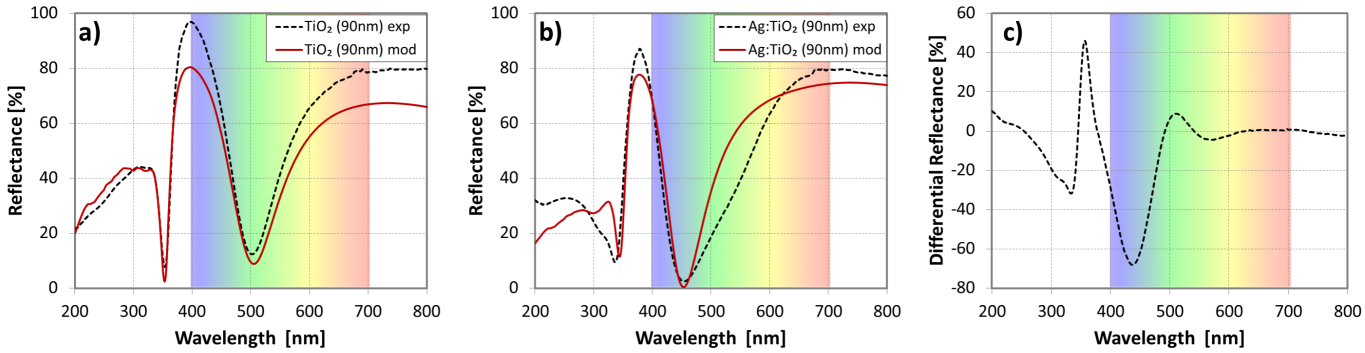

Fig. 4 Reflectance of sample A (experiment in black dotted lines, modelling in continuous red curves). a) non-implanted zone; b) implanted; c) differential reflectance.

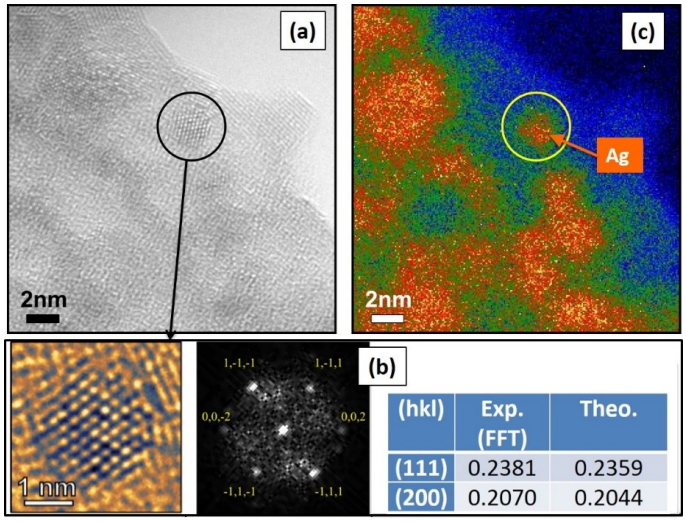

Fig. 3 a) HREM image of the implanted region, close to the free surface, showing the presence of crystalline Ag NPs (see zoom); b) associated FFT of the individual Ag NP shown in the zoom. The NP is oriented following (110) zone axis and the measured interplane distances d_{hkl} fit well with the theoretical values (all in nm); c) EFTEM image (filtering at the 467 eV edge of Ag) in the same region. Ag-rich regions are coloured in orange.

ment in the dielectric layer, as expected (Fig. 1). The presence of silver also induces supplementary absorption corresponding to electronic interband transitions at wavelengths lower than the corresponding threshold near 320 nm (3.9 eV). This is brought out clearly in the differential reflectance spectrum (Fig. 4c) obtained by subtracting the experiment spectrum of a non-implanted zone from that of an implanted zone (Figs. 4a and 4b, respectively). In Fig. 4c, besides the LSPR effect in the visible range, one also observes that the reflectance is reduced in the UV range (250-350 nm). This is a signature of intrinsic absorption by silver but also by defects generated in titania owing to the implantation process[24].

To account more precisely of these effects, simulations have been performed. The dielectric response of the composite layer with Ag NPs embedded in TiO_2 (TiO_2:Ag), has been described by using the quasi-static approximation of the classical Maxwell-Garnet theory (for more details, see[18,19]). The energy relaxation of the plasmon occurs via generation of electron-hole excitations, and the corresponding energetic damping parameter is well known to be given by[25]:

$$\Gamma = \hbar \frac{v_F}{L_{eff}} \qquad (2)$$

where v_F is the Fermi velocity and L_{eff} the effective mean free path for electron collisions. In nm-sized NPs, surface collisions dominate and according to various models $0.43D < L_{eff} < 0.82D$ for a sphere of diameter D[26]. Thus, the electronic confinement effect in the NPs with a mean size D is accounted for by introducing in the imaginary part of the metal dielectric function a plasmon damping term varying as D^{-1}. The best fit reported in Fig. 4b has been obtained by considering the following stacking: $Si/SiO_2(84\,nm)/c{-}TiO_2(68\,nm)/a{-}TiO_2(10\,nm)/a{-}TiO_2{:}Ag(10\,nm)$ in agreement with TEM observations (Fig. 2). The theoretical curve corresponds to Ag NPs mean diameter $D = 3\,nm$, in good agreement with TEM observations. The general trends of the experimental spectra are accounted for, namely the blue shift and deepening of the reflectance minima and the absorption enhancement in the UV mid-range. Nevertheless, some discrepancies are observed in the UV deep-range (below 300 nm) and in the visible mid-range. They are certainly due to the fact that disorder and defects into the TiO_2 matrix are not considered in our model. Indeed very recent works on Fe^{2+} or C^+ implanted TiO_2 films[24] have demonstrated an absorption enhancement in the UV range, and also new absorbing bands in the visible range because the implantation process generates energetically-deep levels into the gap of titania.

The main conclusion of this optical analysis is that embedded Ag NPs can considerably increase the absorption in a titania layer. When the size of these NPs remains in the nanometer range, their interaction with light is indeed dominated by absorption[25] and the LSPR covers a wide spectral range in the visible (Fig. 1). Moreover one can take simultaneously advantage of optical amplification because these Ag NPs are located in the vicinity of the free surface where the electric field is at maximum under anti-reflective conditions[18,19]. More precisely, from data reported in Fig. 4c, one can estimate that a thin layer of 3 nm-sized Ag NPs

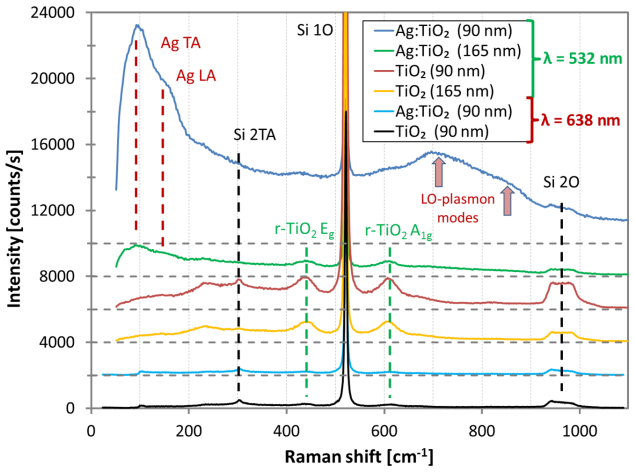

Fig. 5 Raman spectra recorded on non-implanted zones and implanted zones of samples A and B under plasmon-resonant excitation (532 nm) or out of resonance (638 nm). The laser power was the same for all the spectra and limited to ≈ 1 mW to avoid any heating of the samples.

into the composite layer leads to an average absorption increase of around 20 % in the UV-VIS wavelength range.

3.3 Raman spectroscopy in Ag NPs and TiO_2.

We have performed Raman spectroscopic measurements to analyze vibrational modes of the Ag NPs, TiO_2 matrix and Si substrate, but more particularly electron-hole excitations [18]. Moreover plasmon-resonant Raman spectroscopy has been used to get information on electron-phonon interactions in the Ag NPs and in TiO_2. A representative set of Raman spectra recorded on non-implanted zones and implanted zones of samples A and B, under plasmonic-optical resonance conditions (532 nm laser line) or out of resonance (638 nm laser line), are reported in Fig. 5. At first glance, one observes that the lowest signal is obtained with the 638 nm line whatever the zone or sample (similar records on sample B are not reported). This signal consists in the well-known first-order peak and acoustical or optical second-order Raman bands of the Si substrate (referred as 1O, 2A or 2O in Fig. 5, respectively). This signal will be used as a reference for evaluating absorption and resonance effects into the SiO_2/TiO_2:Ag multilayer film deposited on this substrate.

In Fig. 5, the Raman spectra recorded with the 532 nm laser line on non-implanted zones of samples A and B, show the appearance of two well-defined peaks located at 440 and 608 cm^{-1} characteristic of Eg and A1g modes of a crystalline rutile phase of TiO_2 [27]. These peaks are superimposed to a broad band with a cut-off around 700 cm^{-1} that can be attributed to an amorphous-like TiO_2 phase [28]. Thus the Raman assignments comforts the TEM observation revealing a highly disordered polycrystalline film near the surface. The predominance of the rutile phase was expected, due to the preparation procedure of this film [29]. Furthermore, rutile is the most thermodynamically stable and chemical resistant titania phase [30]. One also notes that the signal of Si is rather unchanged due to the transparency preservation of the deposited dielectric film. The most striking point is the fact that the TiO_2 signal drops by about 2 from sample A to B whereas the thickness of TiO_2 is almost doubled (from 85 to 165 nm). This is well accounted for by the optical confinement effect in the dielectric film: only in sample A, the exciting wavelength (532 nm) rather well fulfils the anti-reflectivity condition ($\lambda_{1A} \approx 500$ nm, Fig. 3a). The electromagnetic energy is thus essentially confined in the TiO_2 layer because of its high refractive index value and position near the free surface. In sample B, the optical amplification is very low because the photon wavelength is far from the antireflective condition ($\lambda_{1B} \approx 760$ nm).

This Raman analysis shows how engineering the optical properties of a photocatalytic film can be useful to increase the photon capture in a given spectral range. It is of importance to note that this capture should be better increased by using the lowest order $m = 0$ of antireflective condition and optimizing the multilayer composition.

The Raman spectra recorded with the 532 nm line on implanted zones of samples A and B are displayed in Fig. 5. The spectra are very similar taking into account the optical amplification effect: here the gain is 3.4. The incorporation of Ag in TiO_2 (which is exactly the same in both samples) considerably affects the Raman signal in three main points. First, the signal of the Si substrate is reduced testifying the absorption increase into the metal-dielectric composite film. Second, the peaks characteristic of crystalline rutile have weakened and widened because of disorder-induced effects of the matrix (amorphous-like layer in Fig. 2). Third, new and intense bands appear at low (below 200 cm^{-1}) and at high frequency (between 650 and 900 cm^{-1}). At low frequency they are attributed to Ag vibrational modes, and at high frequency to TiO_2 vibrational modes, respectively. They are superimposed on a continuous background spanning a very large frequency range well beyond the vibrational response cut-off of the composite film near 1000 cm^{-1}.

All these observations are characteristic of a plasmonic-resonant effect, in which the Raman scattering by vibrations is considerably enhanced if the corresponding bonds are located in the vicinity of metallic particles supporting a LSPR. Moreover, such a SERS signal is systematically accompanied by the so-called *background* which origin is generally largely ignored and arbitrary subtracted. However, when photoluminescence processes can be discarded, this background is now recognized as originating in inelastic scattering by electron-hole excitations [18,31–33]. In fact it can be used as a sensitive probe to directly inform on the presence of free carriers. Single-particle excitations consist in intraband transitions for electrons in the vicinity of the Fermi level to the continuum of free states above this level: their spectrum begins at zero frequency and displays a monotonous shape that culminates at a frequency directly linked to the characteristic scale of the electronic confinement [18,31]. For confinement at the nanoscale, the spectral energetic range of electronic excitations coincide with that of many molecular vibrations, ensuring easy tuning for efficient coupling. In sample A, the background ends at a frequency near 2000 cm^{-1} (spectrum not shown here) in good agreement with previous observations in nm-sized Ag NPs [18]. Thus any vibrational mode with a lower frequency may couple with the con-

tinuum of electron-hole excitations of the Ag NPs and thus display a SERS enhancement. Two types of modes are indeed implied, the *bulk* phonons of the Ag NPs themselves and the TiO_2 phonons of the matrix in the vicinity of these Ag NPs. It has been recently shown[18,34] that Raman scattering by bulk phonons of Ag and Au nanocrystals can be activated due to the lack of translational invariance during the light-matter interaction. The signal mimics rather well the vibrational density of states (VDOS) of crystalline nanocrystals and is a powerful tool for structure determination of metal nanoparticles with few nanometers in size[35]. In Fig. 5, one clearly observes two Van Hove singularities of this VDOS corresponding to transverse and longitudinal acoustical modes (TA and LA respectively) at high symmetry points of the Brillouin zone in bulk silver[18]. The strong decrease upon frequency shift is simply due to the Bose population factor effect. The very high intensity of this Raman signal is directly linked to the plasmon-resonant SERS and the high quality factor of the LSPR in titania; it is unobservable out of resonant condition, as shown in Fig. 5.

3.4 LO-phonon-plasmon modes in TiO_2

In Fig. 5 we attribute the structures emerging from the background between 650 and 900 cm^{-1} to enhanced Raman scattering by coupled *LO-phonon-plasmon modes* of TiO_2. This signal is absent out of resonance and without Ag NPs. The coupling of electronic excitations with the longitudinal optical (LO) polar phonons has been widely studied in n- or p-doped semiconductors[36,37] and high-Tc superconductors[38]. These modes have been also observed with IR reflectance spectroscopy in non-stoichiometric rutile[39] and anatase[40,41]. LO- and surface optic (SO-) plasmon modes have also been invoked as sensitive to water absorption at the surface of photocatalytic TiO_2 particle films[28]. In rutile, the four polar LO modes (3 E_u + 1 A_{2u}) are not Raman active due to their odd symmetry[27]. However these modes can strongly interact with free carriers present in the dielectric matrix. The resulting *LO-phonon-plasmon* modes lead to Raman scattering related to mechanisms (electro-optic or Fröhlich) normally forbidden out of resonance. The presence of disorder may favor these mechanisms owing to breakdown of the wave-vector selection rule.

In IR spectra, similar modes have been accounted for theoretically[40,41] by using a dielectric function $\varepsilon(\omega)$ containing two terms, a first one relative to optical phonons and the second to free carriers. One can write this dielectric function, according to notations used by Mlayah and al.[37] and Groenen and al.[42], as follows:

$$\varepsilon(\omega) = \varepsilon_\infty \left(1 + \sum_{i=1}^{4} \frac{\omega_{p,i}^2}{\omega_{T,i}^2 - \omega^2 + i\gamma_i\omega} + \frac{\omega_p^2}{-\omega^2 + i\gamma_p\omega} \right) \qquad (3)$$

where ε_∞ is the high frequency dielectric constant, $\varepsilon_\infty = n_{vis}^2 \approx 8$ for rutile. For each i-th oscillator of TiO_2, the ionic plasmon frequency $\omega_{p,i}$ is defined from the corresponding LO and TO frequencies, $\omega_{L,i}$ and $\omega_{T,i}$:

$$\omega_{p,i}^2 = \omega_{L,i}^2 - \omega_{T,i}^2 \qquad (4)$$

The damping of each oscillator is taken into account through the parameters γ_i and γ_p. The presence of charge carriers is described by the last (Drude-like) term in Eq. (3) in which ω_p is the plasmon frequency. Obviously $\omega_T = 0$ for free carriers. It should be made clear here that this *plasmon* component invoked in the so-called *LO-phonon-plasmon modes* refers to carriers injected in the TiO_2 matrix and not to the free electron gas of the metallic NPs. For TiO_2 polar modes, large TO-LO splittings have to be considered due to the ionic character of the bonds. At high doping level, the coupling with the resulting over damped electronic oscillation is expected to get broad Raman features in the optical-phonon frequency range[37,43]. The frequencies of LO polar modes in rutile have been estimated at 366, 445, 830 cm^{-1} (E_{u2} modes) and 796 cm^{-1} (A_{2u})[44] and thus one expect LO-phonon-plasmon modes in this frequency range, as already observed experimentally in IR spectra[40,41]. Of particular relevance is the fact that Warren and al.[28] have observed the appearance of three modes at 685, 745 and 828 cm^{-1} in IR spectra of TiO_2 photocatalytic particle films. The absorption spectrum is deduced from the imaginary part of the dielectric function, $\Im(\varepsilon(\omega))$ whereas the Raman spectrum is linked to $\Im(-\varepsilon^{-1}(\omega))$. However, in both spectra the frequencies of the *LO-phonon-plasmon* modes are expected near the poles of $\varepsilon(\omega)$ (Eq. (3)). Indeed, an intense and broad Raman band is observed in Fig. 5 near 700 cm^{-1} with a shoulder near 820 cm^{-1}. When several polar modes are simultaneously present in a given material, it has been shown that the higher the frequency is, the stronger the ionic plasmon coupling is[42,45]. In TiO_2, one thus expect that the LO-plasmon coupling will mainly concern the highest frequency and intense E_{u2} mode which TO-LO splitting is 500-830 cm^{-1}.

The presence of broad Raman bands in disordered TiO_2 materials has been observed but attributed to an amorphous-like phase[45]. Here we have discarded such interpretation because the Raman bands lie at higher frequencies than in amorphous titania. We have recorded the Raman spectrum from an amorphous layer of titania deposited on a quartz substrate (not shown here), and have confirmed the presence of a cut-off frequency near 680 cm^{-1} and found a very low scattering efficiency within the same experimental conditions. Moreover the Raman lineshape in Fig. 5 does not reflect the rutile VDOS expected from lattice dynamics simulations[44,46]: only the highest frequency and polar modes are selectively activated. In particular, one notes in Fig. 5 that the E_g and A_g modes are not at all affected by this SERS effect.

Of importance is to note that the enhancement of the polar modes gets a proof of the presence of free carriers into the TiO_2 matrix in the vicinity of Ag NPs. This should offer a very interesting opportunity to analyze in-situ electron transfer from metallic NPs to a polar semiconductor which is known as the crucial step for plasmon-assisted photocatalytic processes.

3.5 Electron-phonon confinement in Ag NPs

Finally, we have used plasmon-enhanced Raman scattering to get information on the Ag NPs sizes, in a nondestructive way. Very low frequency Raman (or Brillouin) spectra have been recorded in plasmon resonant conditions using the 530 nm laser line of a

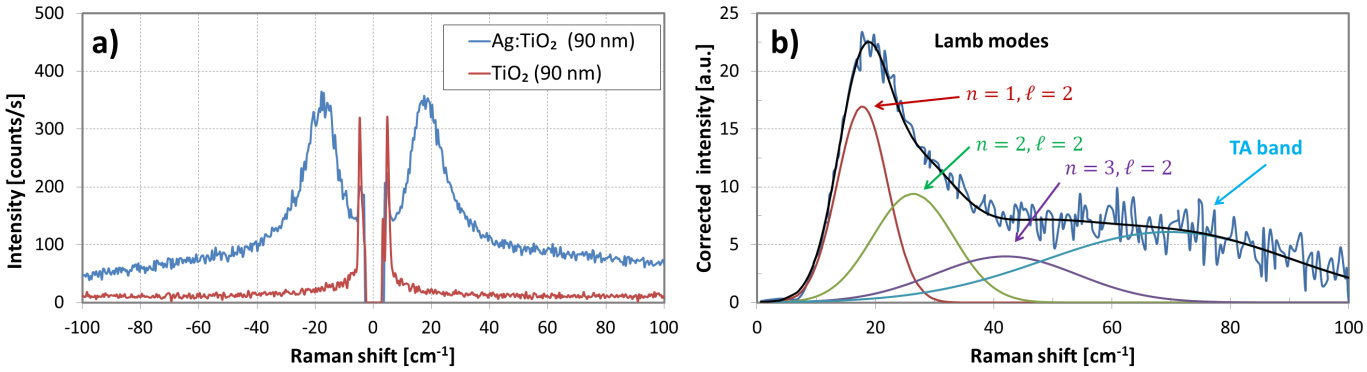

Fig. 6 a) Raman-Brillouin scattering (Stokes and anti-Stokes parts) of an implanted (upper curve, in blue) and non-implanted zone (in red) of sample A under plasmon-resonant conditions (532 nm). b) Deconvolution of the corrected Stokes Raman spectrum into the different (n,ℓ) Lamb modes.

Krypton laser and a specific spectrometric set-up (see Bayle and al.[18] for details). Both Stokes and anti-Stokes parts of the spectra recorded on implanted and non-implanted zones of sample A are reported in Fig. 6a. On silver-free TiO_2 layer, one only observes the Brillouin peak of the Si substrate, whereas on TiO_2 doped with Ag NPs, a very intense Raman band is observed. We interpret this band as due to Lamb modes of the Ag NPs which are strongly enhanced in plasmon-resonant conditions. The intensity of the electron-phonon coupling is at maximum for these vibrational modes because they imply the NP as an ensemble: they are thus spatially coherent with the plasmon mode[18].

These collective oscillations have been already widely studied, either experimentally or theoretically, in Ag or Au NPs embedded in various matrices (Al_2O_3 or SiO_2)[18,47]. It has been shown that only even modes are Raman active, and that the spectrum is dominated by the fundamental ($n=1$) quadrupolar ($\ell=2$) mode. The unusual huge signal observed here in TiO_2 (for the first time to our knowledge) demonstrates once more the high quality factor of LSPR for Ag NPs embedded in a high index matrix.

To get a more precise information from this low-frequency Raman signal, it has been corrected from the set-up response, Bose statistics factor and electron-hole contribution using a procedure already reported[18]. The resulting corrected spectrum is reported in Fig. 6b where the signal has been decomposed in 4 components. A fitting procedure has been performed using Gaussians in order to take into account the inhomogeneous broadening due to statistical size distribution of the Ag NPs. The lowest frequency components, at 17 ± 2, 26 ± 4 and $42\pm8\,cm^{-1}$, are attributed to the lowest harmonics ($n=1$, 2 and 3, respectively) of the quadrupolar Lamb mode ($\ell=2$)[18]. The higher mode (around $70\,cm^{-1}$) is the contribution of the TA band of the silver VDOS, as shown in Fig. 5. The frequencies of these quasi-confined collective modes vary as D^{-1}:

$$\omega_{n,\ell} = A_{n,\ell}\frac{v_T}{D} \qquad (5)$$

where v_T is the transverse sound velocity and $A_{n,l}$ a numerical coefficient depending on the mode and its degree of confinement. For the fundamental quadrupolar mode and using previous calculations[47], one gets $\omega_{1,2}(cm^{-1}) = 47/D(nm)$. That leads to an average size of the Ag NPs $D = 2.8\pm0.3$ nm in good agreement with TEM observations (See Fig. 3) and reflectance simulations.

Low-frequency Raman spectroscopy can thus be used as a non-destructive probe to analyze metallic particles, whose size and location are crucial parameters to define spectrally and spatially the LSPR.

3.6 Electron-hole generation and transfer: photocatalytic activity

From discoloration tests of MB solutions, the photocatalytic activity of implanted samples have been compared with that of non-implanted ones. The results (not reported in details here) do not show an activity enhancement induced by the implantation process and the presence of Ag NPs. On the contrary, a strong reduction ($\approx 80\%$) is observed under UV illumination, probably due to charge carrier recombination on defects generated by the implantation process: the superficial and active layer became a highly disordered TiO_2 phase, as revealed by TEM (Fig. 2) and optical absorption analysis (Fig. 4b). The ion bombardment affects the free surface and thus may alter the MB molecule adsorption efficiency. However the photocatalytic activity under visible illumination is less reduced ($\approx 20\%$). One may argue that disorder effect (traps and surface alteration) is partly compensated in this optical range by Ag NPs plasmonic enhancement effect.

In a very recent work, Liu et al.[13] have deposited Ag NPs on TiO_2 nano-sheet films and measured the hydrogen yield of photocatalytic water splitting under UV and visible light. They conclude that the Ag NPs greatly enhance the photocatalytic activity of anatase TiO_2 and interpret this enhancement as a synergistic effect between charge-transfer and LSPR. They performed Raman measurements and their spectra (Fig. 7 in Liu and al.[13]) clearly reveal that the presence of Ag NPs induces new intense TiO_2 modes between 700 and 900 cm^{-1}, superimposed on a background. These features are very similar to those we ascribe in our work to scattering by LO-phonon-plasmon modes in TiO_2 and single particle excitations in Ag NPs, respectively. The authors gave no specific comment, but interestingly one can note that rising the amount of Ag correlates with rising the intensity of these modes and rising hydrogen yield enhancement.

Although the elaboration conditions of the composite layers were different in both cases, one gathers that plasmon resonant Raman scattering is similarly indicative of migration of carriers from Ag NPs to the semiconducting matrix, according to processes (*i* to *iii*) of the photocatalytic reaction, as presented in Section 1. However, only in the latter case[13] the final process (*iv*) preserves the benefit of the preceding steps.

4 Conclusions

In this work we have shown how a specific optical engineering of composite substrates containing Ag NPs embedded in a thin TiO_2 layer may be fruitful for plasmon-enhanced photocatalytic applications. For that purpose, we have simultaneously taken benefit of the (*i*) very high quality factor of the corresponding localized surface plasmon polariton resonance that guaranties the best electromagnetic field enhancement, (*ii*) downshift versus the middle range of the visible spectrum of this resonance.

Using low-energy ion beam synthesis, Ag NPs have been formed, in a single step procedure, at few nanometers from the free surface, *i.e.* in the region where all the photocatalytic processes take place. At the same time, dissemination of Ag NPs and/or Ag^+ ions -which are known for their toxicity- is avoided.

Moreover, the plasmonic effect is amplified using an antireflective multilayer. This allows to (*i*) increase the photon capture in a desired spectral range and (*ii*) enhance this capture in a very thin layer near the surface.

Finally we have shown that crucial parameters (mean particle size, carrier injection amount, field enhancement factor) for a better knowledge and engineering of elementary processes, can be achieved using plasmon-resonant Raman spectroscopy.

Using simultaneously small Ag NPs (few nanometers in size) in doped titania and the lowest optical interference order in controlled stacking architectures can considerably improve photocatalytic performance under visible light irradiation. These composite substrates which design is optimized so as to maximize the electromagnetic energy and carriers generation also appear promising for sensitive SERS probes or other plasmo-electronics based devices.

References

1 M. A. Shannon, P. W. Bohn, M. Elimelech, J. G. Georgiadis, B. J. Mariñas and A. M. Mayes, *Nature*, 2008, **452**, 301–10.

2 S. Malato, P. Fernández-Ibáñez, M. Maldonado, J. Blanco and W. Gernjak, *Catalysis Today*, 2009, **147**, 1–59.

3 M. N. Chong, B. Jin, C. W. K. Chow and C. Saint, *Water research*, 2010, **44**, 2997–3027.

4 X. Li, J. Yu, J. Low, Y. Fang, J. Xiao and X. Chen, *J. Mater. Chem. A*, 2015, **3**, 2485–2534.

5 A. Fujishima, T. N. Rao and D. A. Tryk, *Journal of Photochemistry and Photobiology C: Photochemistry Reviews*, 2000, **1**, 1–21.

6 K. Awazu, M. Fujimaki, C. Rockstuhl, J. Tominaga, H. Murakami, Y. Ohki, N. Yoshida and T. Watanabe, *Journal of the American Chemical Society*, 2008, **130**, 1676–80.

7 S. D. Standridge, G. C. Schatz and J. T. Hupp, *Journal of the American Chemical Society*, 2009, **131**, 8407–9.

8 S. Linic, P. Christopher and D. B. Ingram, *Nature materials*, 2011, **10**, 911–21.

9 K.-H. Chen, Y.-C. Pu, K.-D. Chang, Y.-F. Liang, C.-M. Liu, J.-W. Yeh, H.-C. Shih and Y.-J. Hsu, *The Journal of Physical Chemistry C*, 2012, **116**, 19039–19045.

10 W. Hou and S. B. Cronin, *Advanced Functional Materials*, 2013, **23**, 1612–1619.

11 M. Dahl, Y. Liu and Y. Yin, *Chemical Reviews*, 2014, **114**, 9853–9889.

12 V. Scuderi, G. Impellizzeri, L. Romano, M. Scuderi, M. V. Brundo, K. Bergum, M. Zimbone, R. Sanz, M. A. Buccheri, F. Simone, G. Nicotra, B. G. Svensson, M. G. Grimaldi and V. Privitera, *Nanoscale*, 2014, **6**, 11189–11195.

13 E. Liu, L. Kang, Y. Yang, T. Sun, X. Hu, C. Zhu, H. Liu, Q. Wang, X. Li and J. Fan, *Nanotechnology*, 2014, **25**, 165401.

14 D. B. Ingram and S. Linic, *Journal of the American Chemical Society*, 2011, **133**, 5202–5.

15 A. Bumajdad and M. Madkour, *Physical chemistry chemical physics : PCCP*, 2014, **16**, 7146–58.

16 R. Long and O. V. Prezhdo, *Journal of the American Chemical Society*, 2014, **136**, 4343–54.

17 D. B. Ingram, P. Christopher, J. L. Bauer and S. Linic, *ACS Catalysis*, 2011, **1**, 1441–1447.

18 M. Bayle, P. Benzo, N. Combe, C. Gatel, C. Bonafos, G. Benassayag and R. Carles, *Physical Review B*, 2014, **89**, 195402.

19 R. Carles, C. Farcau, C. Bonafos, G. Benassayag, M. Bayle, P. Benzo, J. Groenen and A. Zwick, *ACS Nano*, 2011, **5**, 8774–8782.

20 J. Biersack and L. Haggmark, *Nuclear Instruments and Methods*, 1980, **174**, 257–269.

21 A. Mills, C. Hill and P. K. Robertson, *Journal of Photochemistry and Photobiology A: Chemistry*, 2012, **237**, 7–23.

22 R. Carles, C. Farcau, C. Bonafos, G. Benassayag, B. Pécassou and A. Zwick, *Nanotechnology*, 2009, **20**, 355305.

23 A. Bendavid, P. Martin, A. Jamting and H. Takikawa, *Thin Solid Films*, 1999, **355-356**, 6–11.

24 G. Impellizzeri, V. Scuderi, L. Romano, P. M. Sberna, E. Arcadipane, R. Sanz, M. Scuderi, G. Nicotra, M. Bayle, R. Carles, F. Simone and V. Privitera, *Journal of Applied Physics*, 2014, **116**, 173507.

25 C. F. Bohren and D. R. Huffman, *Absorption and scattering of light by small particles*, 1983.

26 E. A. Coronado and G. C. Schatz, *The Journal of Chemical Physics*, 2003, **119**, 3926.

27 J. G. Traylor, H. G. Smith, R. M. Nicklow and M. K. Wilkinson, *Physical Review B*, 1971, **3**, 3457–3472.

28 D. S. Warren and A. J. McQuillan, *The Journal of Physical Chemistry B*, 2004, **108**, 19373–19379.

29 P. Löbl, M. Huppertz and D. Mergel, *Thin Solid Films*, 1994, **251**, 72–79.

30 D. A. H. Hanaor and C. C. Sorrell, *Journal of Materials Science*, 2010, **46**, 855–874.

31 R. Monreal, F. Flores, Y. Gao and T. López-Ríos, *Europhysics Letters (EPL)*, 1987, **4**, 115–120.

32 W. Akemann and A. Otto, *Surface Science*, 1994, **307-309**, 1071–1075.

33 H. Portales, E. Duval, L. Saviot, M. Fujii, M. Sumitomo and S. Hayashi, *Physical Review B*, 2001, **63**, 233402.

34 M. Bayle, N. Combe, N. M. Sangeetha, G. Viau and R. Carles, *Nanoscale*, 2014, **6**, 9157–65.

35 H. E. Sauceda and I. L. Garzón, *The Journal of Physical Chemistry C*, 2014, Article ASAP.

36 A. Mooradian and G. B. Wright, *Physical Review Letters*, 1966, **16**, 999–1001.

37 A. Mlayah, R. Carles, G. Landa, E. Bedel and A. Munoz-Yague, *Journal of Applied Physics*, 1991, **69**, 4064.

38 D. Reznik, S. L. Cooper, M. V. Klein, W. C. Lee, D. M. Ginsberg, A. A. Maksimov, A. V. Puchkov, I. I. Tartakovskii and S.-W. Cheong, *Physical Review B*, 1993, **48**, 7624–7635.

39 J.-F. Baumard and F. Gervais, *Physical Review B*, 1977, **15**, 2316–2323.

40 R. J. Gonzalez, R. Zallen and H. Berger, *Physical Review B*, 1997, **55**, 7014–7017.

41 M. Grujic-Brojcin, M. Scepanovic, Z. Dohcevic-Mitrovic and Z. Popovic, *Science of Sintering*, 2006, **38**, 183–189.

42 J. Groenen, R. Carles, G. Landa, C. Guerret-Piécourt, C. Fontaine and M. Gendry, *Physical Review B*, 1998, **58**, 10452–10462.

43 T. Kozawa, T. Kachi, H. Kano, Y. Taga, M. Hashimoto, N. Koide and K. Manabe, *Journal of Applied Physics*, 1994, **75**, 1098.

44 S. Schöche, T. Hofmann, R. Korlacki, T. E. Tiwald and M. Schubert, *Journal of Applied Physics*, 2013, **113**, 164102.

45 F. D. Hardcastle, H. Ishihara, R. Sharma and A. S. Biris, *Journal of Materials Chemistry*, 2011, **21**, 6337.

46 R. Sikora, *Journal of Physics and Chemistry of Solids*, 2005, **66**, 1069–1073.

47 B. Palpant, H. Portales, L. Saviot, J. Lermé, B. Prével, M. Pellarin, E. Duval, A. Perez and M. Broyer, *Physical Review B*, 1999, **60**, 17107–17111.